Bioactive Materials 12 (2022) 185–197

Contents lists available at ScienceDirect

Bioactive Materials

journal homepage: www.keaipublishing.com/en/journals/bioactive-materials

Nidogen1-enriched extracellular vesicles accelerate angiogenesis and bone regeneration by targeting Myosin-10 to regulate endothelial cell adhesion

Pengzhen Cheng [a,b,1], Tianqing Cao [a,1], Xueyi Zhao [b], Weiguang Lu [a], Sheng Miao [a], Fenru Ning [c], Dong Wang [a], Yi Gao [a], Long Wang [d], Guoxian Pei [a,**], Liu Yang [a,*]

[a] Department of Orthopedics, Xijing Hospital, Fourth Military Medical University, Xi'an, 710032, China
[b] College of Life Sciences, Northwest University, Xi'an, 710069, China
[c] Department of Neonatology, The First Affiliated Hospital of Xi'an Jiaotong University, Xi'an, 710061, China
[d] Department of Orthopaedics, Chinese PLA General Hospital, Beijing, 100853, China

ARTICLE INFO

Keywords:
Extracellular vesicles
Hydrogel
Nidogen1
Angiogenesis
Bone tissue engineering

ABSTRACT

The technique bottleneck of repairing large bone defects with tissue engineered bone is the vascularization of tissue engineered grafts. Although some studies have shown that extracellular vesicles (EVs) derived from bone marrow mesenchymal stem cells (BMSCs) promote bone healing and repair by accelerating angiogenesis, the effector molecules and the mechanism remain unclear, which fail to provide ideas for the future research and development of cell-free interventions. Here, we found that Nidogen1-enriched EV (EV-NID1) derived from BMSCs interferes with the formation and assembly of focal adhesions (FAs) by targeting myosin-10, thereby reducing the adhesion strength of rat arterial endothelial cells (RAECs) to the extracellular matrix (ECM), and enhancing the migration and angiogenesis potential of RAECs. Moreover, by delivery with composite hydrogel, EV-NID1 is demonstrated to promote angiogenesis and bone regeneration in rat femoral defects. This study identifies the intracellular binding target of EV-NID1 and further elucidates a novel approach and mechanism, thereby providing a cell-free construction strategy with precise targets for the development of vascularized tissue engineering products.

1. Introduction

Repairing large-scale defects such as bone and skin is an intractable clinical problem [1–4]. It has been reported that biological scaffolds loaded with bone marrow mesenchymal stem cells (BMSCs) significantly promote the repair of osteochondral defects [5–8]. Our previous study showed that BMSCs and rat arterial endothelial cells (RAECs) cooperate to regulate the microenvironment of the defect site and promote bone regeneration by accelerate vascularization [9,10], but the regulatory molecules and mechanisms by which BMSCs accelerate vascular regeneration are not clear. In addition, BMSCs have the limitation of infection risk and poor therapeutic effect of aging cells [11]. Therefore, clarifying the mechanism of BMSCs in promoting defect repair will contribute to the development of new tissue engineering products.

Recent studies have suggested that BMSCs play a therapeutic and regulatory role mainly through the paracrine pathway [12–15]. The secretome derived from MSC contains many effector molecules, which could affect cellular characteristics and behavior [16]. Extracellular vesicles (EVs), important carriers of intercellular communication, transport proteins, lipids and RNAs, target cells to perform regulatory functions [17,18]. Compared with cell therapy, EVs have a low risk of pathogenic infection and tumorigenesis, indicative of the potential to become an ideal bioremediation agent [19–22].

Nidogen1 (NID1) is an extracellular matrix (ECM) protein mainly secreted by stromal cells. NID1 consists of three globular domains (G1, G2 and G3), that bind to collagen IV and laminin in the ECM [23–25], and maintain microenvironment homeostasis as a structural protein [26]. NID1 is demonstrated to be an important component of the vascular basement membrane (BM) [27], and provides the structural and mechanical features that support the endothelium and vascular

Peer review under responsibility of KeAi Communications Co., Ltd.
* Corresponding author.
** Corresponding author.
E-mail addresses: nfperry@163.com (G. Pei), yangliu@fmmu.edu.cn (L. Yang).
[1] These authors contributed equally to this work.

https://doi.org/10.1016/j.bioactmat.2021.10.021
Received 12 July 2021; Received in revised form 15 October 2021; Accepted 18 October 2021
Available online 27 October 2021

integrity [28]. A recent study reported that NID1 attenuated the apoptotic effect of cardiomyocytes and pancreatic β-cells via the αvβ3 integrin [29], suggesting that NID1 has the potential to regulate cell biological functions as a signaling molecule. However, the underlying mechanism of NID1 as signaling molecule has not been revealed.

This study identified a novel existence and secreted form of NID1 derived from BMSC, namely EV-NID1, and EV-NID1 was shown to interfere with the formation and assembly of focal adhesions (FAs) by targeting myosin-10, thereby reducing the adhesion strength of rat arterial endothelial cells (RAECs) to the ECM, and enhancing the migration and angiogenesis potential of RAECs. In addition, EV-NID1 was loaded into a sodium alginate/PEG2000/gelatin composite hydrogel and implanted into the rat femoral defect site to further evaluate the repair effect of EV-NID1 *in vivo*. The results confirmed that EV-NID1 promotes angiogenesis and bone regeneration, providing a cell-free construction strategy with precise targets for the development of vascularized tissue engineering products.

2. Materials and methods

2.1. Adhesion rate detection

The detection operation was performed according to the instructions of the cell adhesion kit (Bestbio, BB-48120, China).

2.2. Acquisition and characterization of EVs

When the cell fusion rate reached approximately 85%, the medium containing 10% exosome-free serum (VivaCell Biosciences, China) was replaced and incubated for 48 h. The EVs in the cell supernatant were extracted by ultracentrifugation [30]. Nanoparticle tracking analysis (NTA) of EVs was performed using a NanoSight instrument (PARTICLE METRIX, ZetaVIEW S/N17-310, Germany).The morphology and structural integrity were visualized using a transmission electron microscope (TEM, H-9500, Hitachi). The biological markers of EVs in each group were detected by Western blot. For EVs samples, loading buffer was directly added to mix with EVs solution and heated until protein denaturation. It is not necessary to extract total protein with lysate. The primary antibodies were as follows: CD9 (Abcam, ab92726, UK, 1:1000), HSP90 (Abcam, ab32568,UK, 1:1000), CD63 (SBI, EXOAB-CD63A-1, USA, 1/1000), and TSG101 (Abcam, ab125011, UK, 1:1000).

2.3. Transcriptome sequencing and TMT proteomics

The RNA level changes of RAECs and Co-RAECs were analyzed by transcriptome sequencing (Sangon Biotech, China), with 3 biological replicates in each group. Proteins contained in EVs were determined by TMT Proteomics (KangChen Bio-tech, China), with 2 biological replicates per group.

2.4. In vitro stimulation experiment of EVs on RAECs

In recent years, nanoparticle tracking analysis (NTA) has been proven to be an effective technology for qualitative and quantitative analysis of EVs. Therefore, follow-up experiments were performed with the particle concentration as the design standard. The EVs were diluted to concentrations of 10^7, 10^8 and 10^9 particles/mL according to the number of particles, and then added to a six-well plate pre-seeded with RAECs, incubated at 37 °C for 48 h with 5% CO2 for subsequent experiments.

2.5. Matrigel plug test in nude mice

RAECs co-cultured with $BMSCs^{shVector}$ and $BMSCs^{shNID1}$ were digested and resuspended, and the cell density was adjusted to $6x10^6$ cells/mL. 600uL of the cell suspension was added into 150uL of pre-melted matrigel. Furthermore, 10^9 particles/mL EVs and EVs^{shNID1} were added into matrigel, and the same volume of PBS was used as the control. 250uL of the above-mentioned matrigel mixture was injected into the back of nude mice subcutaneous, and the matrigel was solidified after 30S. The vascular regeneration in the matrigel was observed at 14 days post operation.

2.6. NID1 was overexpressed in RAECs and its binding target was determined by IP-MS

RAECs were seeded into six-well plate at the density of $1.5x10^5$ cells/mL. After 12h, 2uL of overexpression adenovirus was added and the samples were collected after 24h/48h/72h incubation for subsequent experiments. According to the results of WB, cells infected with adenovirus for 48 h were selected for IP test. The details of IP experiment referred to previous article [29]. The IP products were separated by narrow-hole high-performance liquid chromatography. Subsequently, automatic Edman degradation sequencing and database comparison analysis were performed on the ABI 477A machine.

2.7. Co-IP confirmed the binding of NID1 and myosin-10

The interaction between NID1 and myosin-10 was verified by IP-NID1 and IP-myosin-10 in Co-RAECs. The dosage of IP antibody was 10uL of anti-NID1 (Proteintech, 13766-1-ap, China) and 8uL of anti-myosin-10 (Proteintech, 19673-1-ap, China).

2.8. Western blots

The operation details were described in our previous research [10]. Proteins were determined using a bicinchoninic acid assay (InCellGene, IC-7991, USA). The primary antibodies were anti-NID1 (Proteintech, 13766-1-ap,China,1:500), anti-myosin-10(Proteintech,19673-1-ap, China,1:200), anti-Rac1/cdc42(Affinity, DF6332,USA,1:1000), anti-Vinculin(Sigma-aldrich,v1931,USA,1:500), anti-Paxillin (Abcam, ab32115, UK, 1:500), anti-FAK (Abcam, ab40794, UK, 1:1000), anti-GAPDH (Elabscience, E-AB-20059, USA, 1:2000).

2.9. Animals

Sprague-Dawley (SD) rats and nude mice were obtained from the experimental animal center of the Fourth Military Medical University. All experimental animals were maintained in the animal facility of the experimental animal center of the Fourth Military Medical University. The experimental protocol was reviewed and approved by the Ethics Committee for Animal Research of Fourth Military Medical University.

2.10. Composite hydrogel preparation

The EVs of 10^8particles/mL was the effective concentration *in vitro*. However, considering the complex microenvironment *in vivo*, the EVs-hydrogel with the concentration of 10^9particles/mL will be constructed in this study. The brief operation details were as follows: pure water, reagents and consumables were sterilized by high temperature or filtration. 0.1g sodium alginate and 0.1g PEG2000 were added into 10 mL pure water, stirred for 1h to dissolve, then 0.4g gelatin was added, stirred and dissolved at 30 °C to obtain mixed prepolymer solution. Then added EVs, EVs^{shNID1} or PBS into the solution, transferred to the mold and solidify naturally within 10 min. Then, 2% CaCl2 solution was used to crosslink for 15 min, the excess CaCl2 was removed by washing with PBS, and implanted into the defect site of the rat femoral condyle.

2.11. Rat femoral condyle defect

The WT-SD rats (male, 12 weeks old, 220 ± 10 g) were randomly

divided into four groups with 12 rats in each group. The experimental animals were fasted overnight before the surgical operation and anesthetized by intraperitoneal injection of 2% w/v pentobarbital sodium salt (30 mg/kg, Merck, Germany). The standard critical cylindrical bone defect (3.5 mm in diameter and 5 mm in depth) was established at the medial femoral condyle. The cylindrical hydrogel was implanted into the bone defect site, and then the muscle and skin were sutured. Afterwards, the rats were kept in SPF environment, and antibiotics (50 kU/kg penicillin) were applied three days after surgery. Meanwhile, the activity and wound healing status of the rats were observed.

2.12. Statistics analysis

Data were presented as the mean ± SD. Comparisons between two groups were accomplished using independent sample T-tests and correlation analysis. Statistical analysis was performed using SPSS 22.0 software. P values < 0.05 were deemed significant, with * representing $P < 0.05$, **$P < 0.01$ and ***$P < 0.001$.

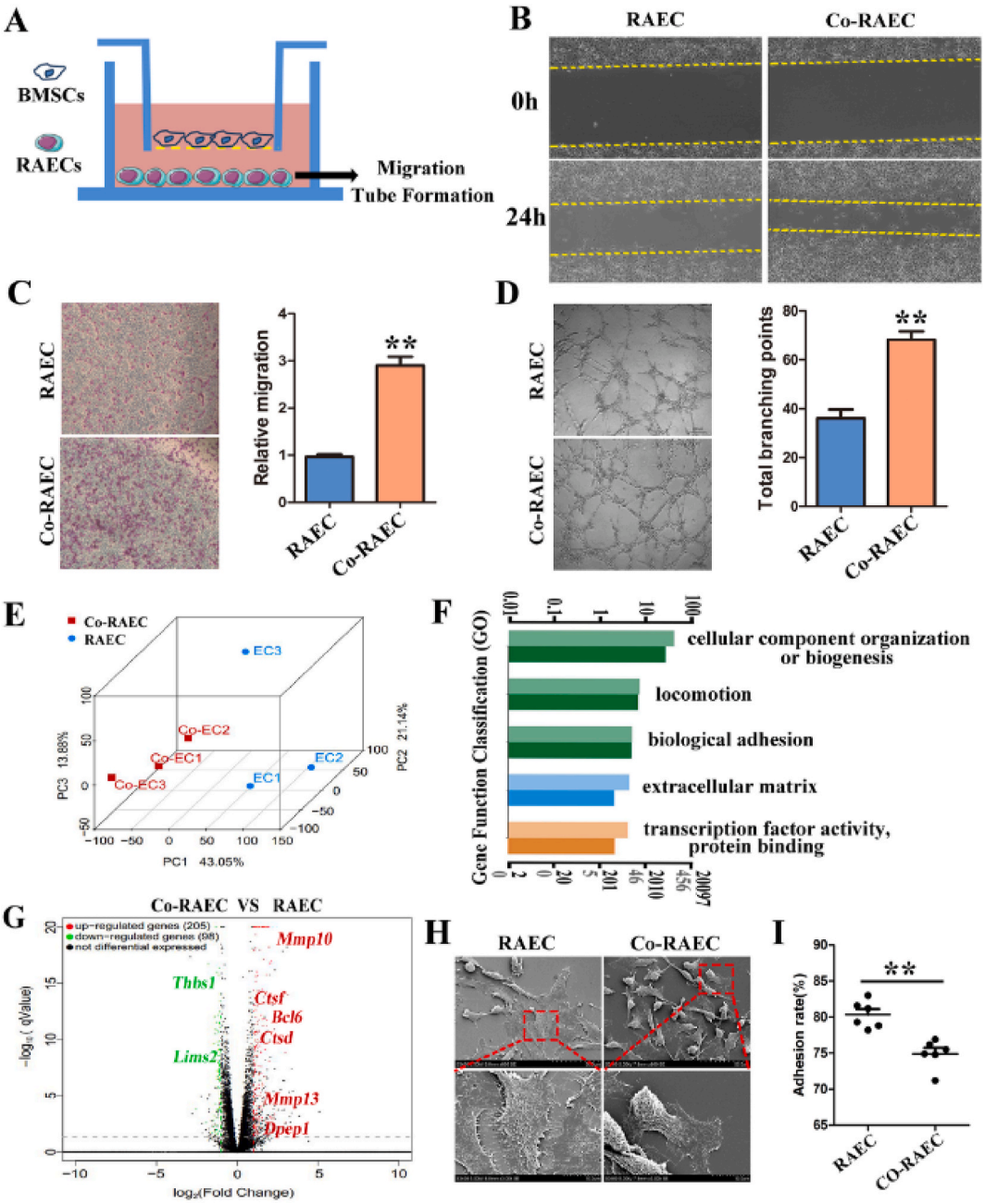

Fig. 1. BMSCs promote the migration and tubule formation of RAECs by regulating cell adhesion. (A) Schematic diagram of Transwell co-culture system of BMSCs and RAECs. (B)The wound healing rate of RAECs and Co-RAECs in 24h. The distance between the yellow dotted lines represents the scratch gap. (C) Transwell assay was used to detect the migration ability of RAECs and Co-RAECs. (D) Tubule formation ability of RAECs and Co-RAECs, and compared the total branching points between the two groups; (E) Principal component analysis (PCA) of the gene changes. (F) Gene function classification analysis diagram of differential genes. Light-colored columns represent differentially expressed genes, and dark-colored columns represent all genes (including differential and non-differential genes). The light-colored column is higher than the dark-colored column, indicating that the significantly differentially expressed genes have an enrichment trend in this term. (G) Differential gene volcano plot of RAECs and Co-RAECs, the red genes was up-regulated relative to RAECs and green means down-regulated genes. (H) The morphology of RAECs and Co-RAECs was observed by scanning electron microscope (SEM). (I) Cell adhesion rate of RAECs and Co-RAECs. Data were represented as the mean ± SD. **$p < 0.01$.

3. Results

3.1. BMSCs regulate the migration, tube formation and adhesion of RAECs in a paracrine manner

To explore the regulatory effect of BMSCs on RAECs, we established a Transwell co-culture system *in vitro* (Fig. 1A, Fig. S1). In the Transwell system, the interaction between BMSCs and RAECs was mediated by the culture medium. The biological phenotypes of RAECs were evaluated by a series of experiments such as wound healing, Transwell migration, and tubule formation in Matrigel. The results showed that the wound healing rate (Fig. 1B), migration (Fig. 1C) and tubule formation abilities (Fig. 1D) of RAECs were significantly enhanced after co-culture with BMSCs. In addition, the early apoptotic cells of co-cultured RAEC (Co-RAEC) were reduced (Figs. S2A and B), and the proliferation capacity was increased (Fig. S2C). To further clarify the changes of gene expression in RAECs after co-culture with BMSCs, transcriptome sequencing of RAECs and Co-RAECs was performed, and principal component analysis (PCA) showed significant changes in Co-RAECs at the transcriptional level (Fig. 1E). Gene Ontology (GO) analysis showed that the differentially expressed genes in Co-RAECs were enriched in the following functional modules: cellular component organization or biogenesis; location; biological adhesion; extracellular matrix; transcription factor activity, protein binding (Fig. 1F). The volcano plot

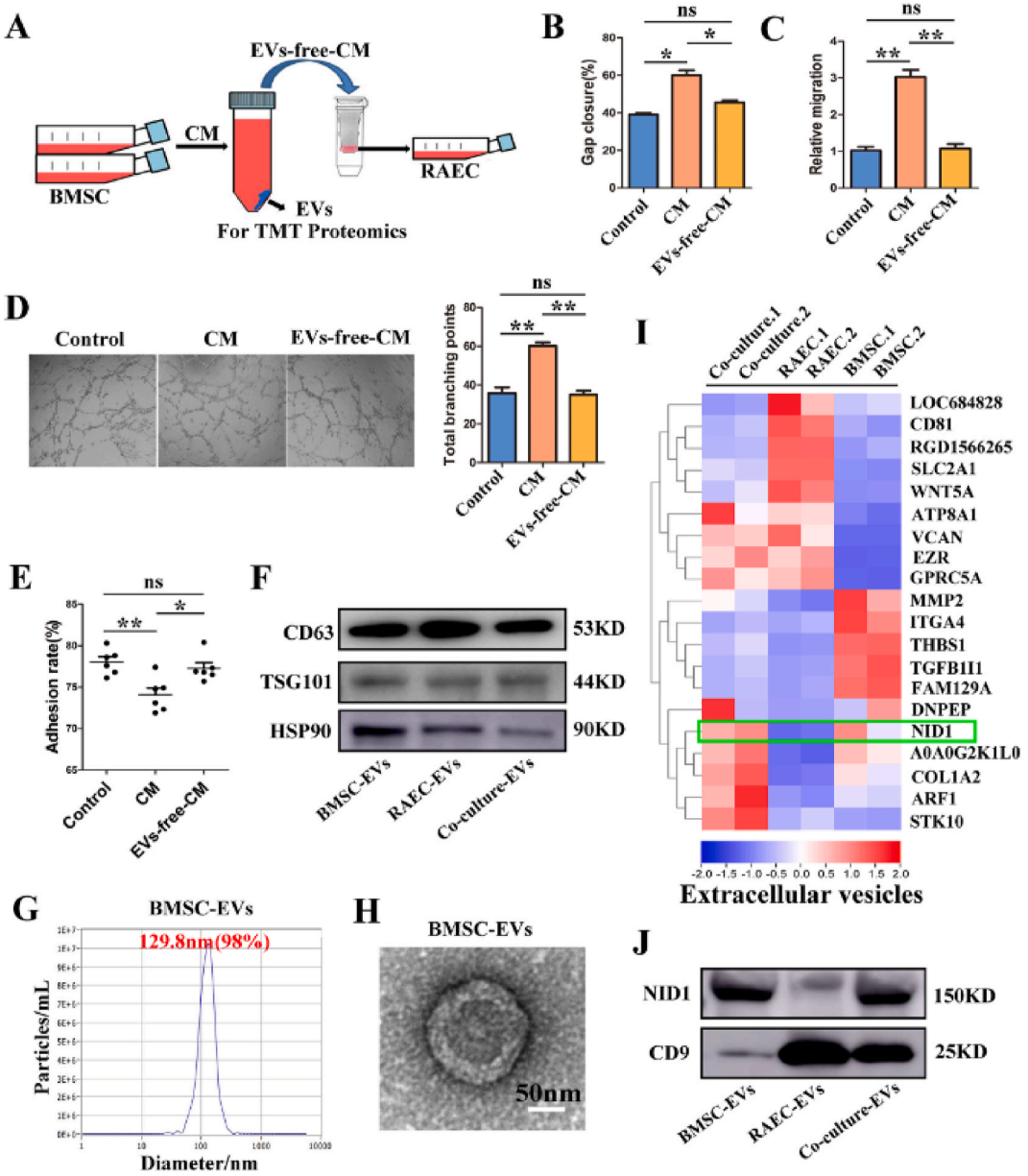

Fig. 2. Nidogen1-enriched EV (EV-NID1) derived from BMSCs may be a key candidate mediator. (A) Schematic diagram of the cytology experiment. RAECs were incubated with concentrated conditioned medium (CM) for 48 h, the EVs were analyzed by TMT proteomics. (B) Wound healing of RAECs incubated with CM or EVs-free-CM (PBS as the Control). (C) Relative migration capacity. (D) Comparison of tubule formation ability and total branching points. (E) The adhesion rate of RAECs in each group. (F) The expression of specific markers (CD63, TSG101 and HSP90) in BMSC-EVs, RAEC-EVs and Co-culture-EVs. (G) Nanoparticle tracking analysis (NTA) showed the particle size distribution of BMSC-EVs. (H) Transmission electron microscopy (TEM) imaging of BMSC-EVs, Scale bar, 50 nm. (I) Heat map of TMT proteomics analysis. The green box indicates that NID1 enriched in BMSC-EVs and Co-culture-EVs, but absented in RAEC-EVs, and was proposed as a candidate effector molecule. (J) The abundance of NID1 in EVs was verified by Western blot. Data were represented as the mean ± SD. *$p < 0.05$; **$p < 0.01$; ns, not significant from Student's t-test.

showed that the expression of genes that positively regulated cell adhesion, such as *Thbs1* and *Lims2*, was significantly down-regulated, while the expression of genes that negatively regulated cell adhesion, such as *Mmp10*, *Mmp13* and *Bcl6*, was significantly up-regulated (Fig. 1G).

We further observed the cell morphology of the two groups by scanning electron microscopy (SEM) and found that the cells in the RAEC group were fully extended and tightly bound to the ECM, while approximately 40% of the cells in the Co-RAEC group had pseudopodia contraction, and these cells became detached and migrated (Fig. 1H). Correspondingly, the adhesion rate of Co-RAECs decreased significantly (Fig. 1I). These results indicated that BMSCs might secrete functional molecules to drive cytoskeletal remodeling of RAECs, weaken the cell-ECM adhesion strength, and thereby promote the migration and tube formation of RAECs.

3.2. NID1 is enriched in EVs derived from BMSCs

To investigate whether BMSCs regulated the biological functions of RAECs through EVs or soluble factors in the supernatant, the conditioned medium (CM) of BMSCs was separated into EVs and EVs-free-CM by ultracentrifugation, and their effects on RAECs were observed respectively. Finally, TMT proteomics was performed to further identify the biological components (Fig. 2A).

Incubation with concentrated CM for 48 h significantly enhanced the wound healing (Fig. 2B, Fig. S3A), migration (Fig. 2C, Fig. S3B) and tubule formation capabilities (Fig. 2D) of RAECs. The results showed that the adhesion rate of RAECs pretreated with CM decreased significantly, which was consistent with the results of co-culture (Fig. 2E). In contrast, the regulatory effect of EVs-free-CM on RAECs was almost negligible (Fig. 2B–E, Fig. S3). Therefore, the regulatory effect of BMSCs on RAECs depended on the biological ingredients in EVs.

EVs derived from BMSCs, RAECs and coculture cells were separated and identified, and then TMT proteomics was performed to explore the core active molecules in EVs. Western blot (WB) analysis showed that EVs in the three groups all expressed CD63, TSG101 and HSP90 (Fig. 2F). Nanoparticle tracking analysis (NTA) indicated that the size distribution of more than 98% of BMSC-EVs was approximately 129 nm (Fig. 2G). Transmission electron microscopy revealed that BMSC-EVs were typically disc-shaped, and their diameter was consistent with the NTA data (Fig. 2H). The particle size distribution and morphology of RAEC-EVs and Co-culture-EVs were similar to those of BMSC-EVs (Figs. S4A and B). Further TMT proteomics analysis showed that NID1 was significantly enriched in BMSC-EVs and Co-culture-EVs, but the content in RAEC-EVs was extremely low(Fig. 2I). It has been reported that NID1 plays an important role in ECM assembly, degradation and neovascularization, suggesting that NID1 may be a candidate active ingredient for BMSCs to regulate RAECs.

In addition, we verified the NID1 content in EVs by WB, with CD9 as an internal reference. The results showed that NID1 was abundant in BMSC-EVs and Co-culture-EVs, but it was almost absent in RAEC-EVs (Fig. 2J). Moreover, NID1 was highly expressed in BMSCs, but expressed at low levels in RAECs (Fig. S4C). The above results suggested that RAECs may capture BMSC-EVs from CM, triggering cytoskeletal remodeling and multiple functional changes.

3.3. EV-NID1 is a key effector molecule of BMSCs regulating RAECs

To confirm that NID1 is the essential mediator of BMSCs regulating RAECs, we knocked down NID1 in BMSCs, and then performed EV incubation and Transwell assays (Fig. S5, Fig. S6) to evaluate the essential role of NID1. The shNID1-2 was first demonstrated to show the highest knockdown efficiency by WB and was selected for subsequent experiments (Fig. S5B).

EVs (EV-NID1) and EVs^{shNID1} were incubated with RAECs for 48 h to explore the regulatory roles of EV-NID1 directly. The WB results confirmed the low expression of NID1 in EVs derived from $BMSC^{shNID1}$ (Fig. 3A), and green fluorescence was observed in the cytoplasm of RAECs after incubation with PKH67-labeled EVs, indicating that EVs were internalized by RAECs (Fig. 3B). In this study, three parallel experiments were performed according to the particle concentrations of EVs, which were 10^7 particles/mL, 10^8 particles/mL and 10^9 particles/mL, respectively. EVs^{shNID1} (10^9 particles/mL) were used as the functional control of EV-NID1.

The results of the wound healing test showed that EVs significantly accelerated the healing of scratches, and this effect was positively correlated with the concentration of EVs, while high concentrations of EVs^{shNID1} did not promote gap closure (Fig. 3C and D). High concentrations of EVs (10^8 particles/mL and 10^9 particles/mL) promoted the migration of RAECs. However, the cell migration ability of the 10^7 particles/mL and EVs^{shNID1} groups was not significantly different from that of the control group (Fig. 3E and F). The results of tubule formation potential were consistent with the migration test results (Fig. 3G and H).

In addition, we found that RAECs incubated with EVs were more sensitive to trypsin. Based on the above results and the transcriptome data of Co-RAECs (Fig. 1G), we speculated that EVs were captured and internalized by RAECs, which led to the decrease of adhesion strength with ECM, thereby enhancing the migration and tube formation capabilities of RAECs. To verify this hypothesis, we measured the cell adhesion rate and the state of FAs. The results showed that with increasing of EVs concentrations, the adhesion rate of RAECs decreased gradually (Fig. 3I). The fluorescence staining images of vinculin/F-actin (Fig. 3J) and paxillin (Fig. S7) clearly showed cytoskeletal reorganization, pseudopodia contraction, FA number reduction in the EV stimulation group, which were mutually confirmed with the adhesion rate results. In contrast, there were no significant changes in the adhesion rate and FAs images of EVs^{shNID1} group, indicating that NID1 in EVs played an important role in regulating RAECs *in vitro*. Furthermore, EVs and EVs^{shNID1} at a concentration of 10^9 particles/mL were loaded into Matrigel (the control group was loaded with the same volume of PBS), and subcutaneously implanted into nude mice to observe vascular regeneration inside the material. Gross observation showed that vascular infiltration in the EVs group was sufficient and significantly better than that in the other two groups. The distribution range of blood vessels in the EVs^{shNID1} group was slightly broader than that in the Matrigel group. HE staining showed that the EVs group had the most vascular-like structures and red blood cell distribution inside, and the number of new vessels in the EVs^{shNID1} group was slightly greater than that in the Matrigel group. CD31 immunohistochemistry also showed that the angiogenic effect of EVs was better than those of the other two groups (Fig. 3K and L). The above experimental results were highly consistent with the phenomenon of Transwell co-culture.

To further verify that NID1 is the key signaling molecule by which BMSCs regulate RAECs, we repeated the above experiments in the co-culture system of $BMSCs^{shNID1}$ and RAECs. First, the low content of NID1 in $BMSCs^{shNID1}$ medium was confirmed by ELISA. Interestingly, the ineffective regulation of RAECs by EVs-free-CM seems to be attributable to its low abundance of NID1 (Fig. S5C). Subsequent Transwell co-culture experiments further confirmed that NID1 plays an important regulatory role in the migration, tube formation, adhesion and angiogenesis of RAECs (Fig. S5, Fig. S6).

These results indicated that NID1 interferes with the cytoskeleton and FA status of RAECs, resulting in a decrease of adhesion strength between RAECs and ECM, which promotes the detachment and then migration of these cells to form a vascular-like structure.

3.4. NID1 regulates FA formation and adhesion to the ECM by targeting myosin-10 in the RAECs cytoplasm

Next, we aimed to identify the downstream target and elucidate the regulatory mechanism of EV-NID1 after internalization by RAECs. Considering the low expression of NID1 in RAECs, we used adenovirus to

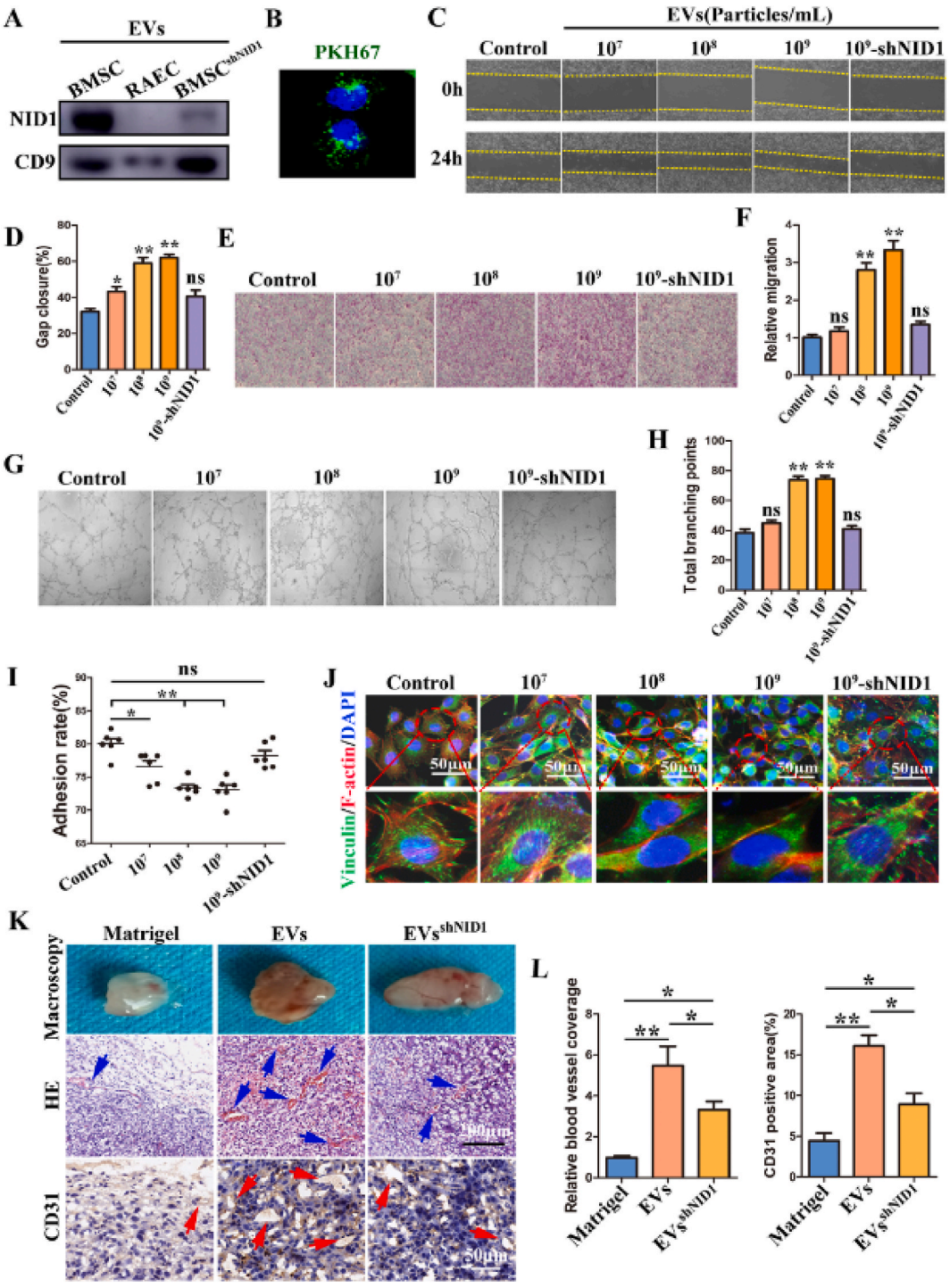

Fig. 3. EV-NID1 significantly enhances the migration and vascularization capabilities of RAECs by regulating cell adhesion. (A) The abundance of NID1 in EVs derived from BMSC, RAEC and BMSC^{shNID1} was determined by WB. (B) PKH67-labeled EVs were internalized by RAECs. (C and D) EVs derived from BMSCs were incubated with RAECs for 48 h, the effect of EVs on the wound healing ability of RAECs was evaluated by scratch experiment. (E and F) Transwell migration assay. (G and H)Tubule formation in Matrigel, and the total branching points were compared statistically. (I)The adhesion rate of RAECs. (J) Immunofluorescence staining images of vinculin and F-actin. (K) The EVs or EVs^{shNID1} with the concentration of 10^9 particles/mL (PBS as control) were loaded into matrigel and subcutaneously implanted into nude mice. The angiogenesis in matrigel was evaluated at 14 days post operation. The blue arrow represents neovascularization, and the red arrow represents CD31$^+$ blood vessels. (L) Comparison of relative vascular coverage and CD31 positive areas in matrigel. Data were represented as the mean ± SD.*$p < 0.05$; **$p < 0.01$; ns, not significant from Student's t-test.

overexpress NID1 and obtained NID1-binding protein by Co-IP, and then identified the binding target by mass spectrometry (MS) and database bioinformatic analysis. WB results showed that the expression of NID1 in RAECs was significantly increased after 48 h of adenovirus infection (Fig. 4A), therefore the 48-h infection group was selected for subsequent experiments and MS analysis.

The results showed that the capacity of wound repair (Fig. 4B, Fig. S8A), migration (Fig. 4C, Fig. S8B) and tubule formation (Fig. 4D, Fig. S8C) in the Ad-NID1 group was significantly enhanced compared with those of the Ad-NC group and control group. In addition,

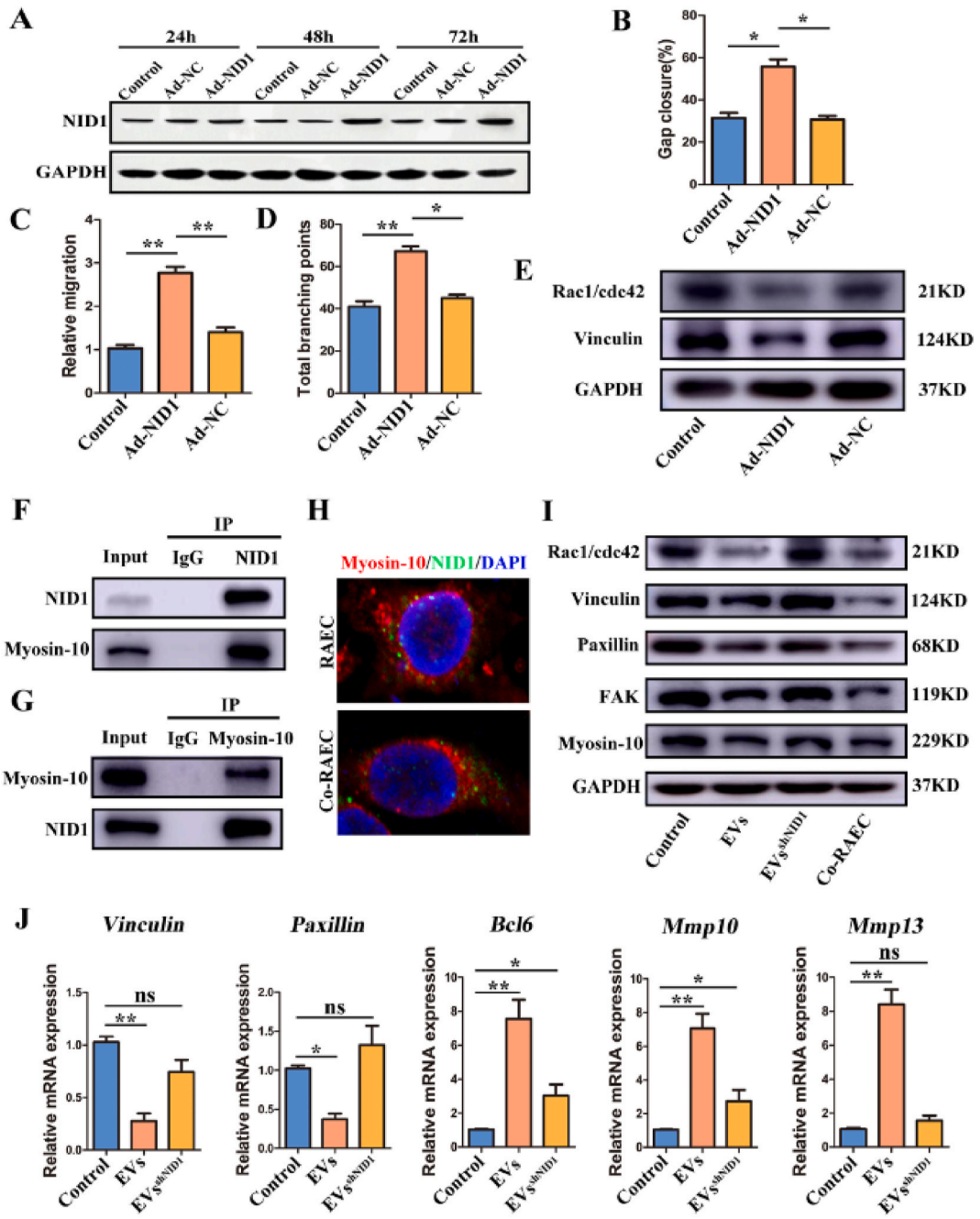

Fig. 4. EV-NID1 regulates the formation and assembly of FAs by targeting myosin-10. (A)Adenovirus was used to overexpress NID1 in RAECs, and the overexpression efficiency was detected by WB. (B) The effect of endogenous overexpression of NID1 (adenovirus infection for 48h) on the wound healing ability of RAECs. (C) The effect of NID1 overexpression on the migration of RAECs. (D) Overexpression of NID1 affected the tubule formation of RAECs. (E) The effects of NID1 overexpression on the expression of Rac1/cdc42 and vinculin. (F)The binding of NID1 and myosin-10 was verified in Co-RAECs. Co-immunoprecipitation of myosin-10 by NID1 antibody. (G) Reverse Co-immunoprecipitation of NID1 by myosin-10 antibody. (H) The intracellular location and distribution of NID1 and myosin-10. (I) The expression of Rac1/cdc42, focal adhesion complex (vinculin/paxillin/FAK) and myosin-10 were measured by WB. Co-RAECs were used as positive control. (J) Relative mRNA expression of *vinculin*, *paxillin*, *BCL6*, *MMP10* and *MMP13* in RAECs. Data were represented as the mean ± SD. *p < 0.05; **p < 0.01; ns, not significant from Student's t-test.

cytoskeleton remodeling, pseudopodia contraction, and FAs were reduced significantly in RAECs overexpressing NID1 (Fig. 4E, Fig. S8D). These results indicated that the phenotype induced by NID1 overexpressing was similar to that in EVs treatment and Transwell co-culture.

MS identification results showed that myosin-10 specific peptides were enriched (Table 1), and its combination with NID1 was highly credible. To further verify the direct binding of myosin-10 and NID1, Co-IP was performed on the total protein of Co-RAECs. Our findings showed that myosin-10 was detected in the Co-IP products of NID1 (Fig. 4F), and NID1 was also detected in the reverse Co-IP product of myosin-10 (Fig. 4G). On the other hand, the myosin-10/NID1 immunofluorescence staining indicated that myosin-10/NID1 was evenly distributed in the cytoplasm of RAECs, while the distribution of myosin-10/NID1 had obvious polarity in Co-RAECs (Fig. 4H). Previous studies have shown that the flow of myosin-10 in the cytoplasm drives the rearrangement of the cytoskeleton, thereby enhancing cell mobility [31,32], which was also suggested by the polarity distribution of myosin-10/NID1 in

Table 1
Mass spectrometry results of IP-NID1 products.

Protein names	Unique peptides	LFQ intensity Ad-NC	LFQ intensity Ad-NID1
CAD protein	10	27039000	129300000
Myosin-10	**65**	**54300000**	**1641700000**
Condensin complex subunit 1	10	32766000	111620000
Enhancer of mRNA-decapping protein 4	2	0	6911700
Nidogen1	17	58000000	22254000000
Putative Polycomb group protein ASXL2	2	739210000	643390000
Neuropathy target esterase	2	0	26648000
FRAS1-related ECM protein 1	1	24194000	0
Myb-binding protein 1A	30	287080000	642650000
ATP-dependent RNA helicase DDX42	2	14243000	48408000
Sulfhydryl oxidase 2; Sulfhydryl oxidase	2	16132000	16872000
Rac GTPase-activating protein 1	2	18228000	0
Ataxin-10	3	25989000	28501000
Calcium/calmodulin-dependent protein kinase type II subunit delta	1	13099000	41674000
ESF1 homolog	4	19589000	26341000
Gamma-enolase; Enolase	8	8919000	123810000
Trophoblast glycoprotein	3	0	20288000
Na(+)/H(+) exchange regulatory cofactor NHE-RF2	3	30002000	9239700
Upstream stimulatory factor 1	2	22883000	17970000
Tetraspanin; CD82 antigen	3	55042000	19234000
Ras-related protein Rab-3B	3	17928000	42974000
Heme-binding protein 1	3	0	25087000
ADP-sugar pyrophosphatase	2	12367000	24798000
40S ribosomal protein S28	2	17716000	11937000
Core-binding factor subunit beta	2	0	22728000

Unique peptides represent the number of characteristic peptides of the target protein. LFQ intensity represents the protein abundance detected by label-free quantification.

Co-RAECs.

Furthermore, we evaluated the changes in the molecular biology of RAECs after internalizing EVs, and used RAECs and Co-RAECs as negative and positive controls. The results showed that the expression of Rac1/cdc42 (an indicator of pseudopodia formation) was significantly reduced after EVs stimulation, corresponding to the pseudopodia contraction results mentioned above. In addition, the expression of the FAK/vinculin/paxillin complex (FA proteins) was decreased significantly(Fig. 4I), which was further confirmed by the fluorescence imaging of FAs in Fig. 3 and Fig. S7, and the overall trend was consistent with that in the Co-RAECs group. However, the phenotypes of the EVs^{shNID1} group and the control (RAECs) group were not obviously changed, further confirming that EV-NID1 was directly involved in the cytoskeletal remodeling and FAs formation in RAECs. WB results also showed that the expression of myosin-10 decreased after RAECs internalized EVs, but there was no significant difference with internalization of EVs^{shNID1} (Fig. 4I). On the other hand, the expression of genes involved in FA formation was significantly down-regulated(*vinculin* and *paxillin*), and that of genes driving cytoskeletal remodeling and ECM degradation (*Bcl6*, *Mmp10*, *Mmp13*) was significantly up-regulated after internalization of EVs, while internalized EVs^{shNID1} had a slight regulatory effect on the expression of these molecular markers(Fig. 4J).

Interestingly, we found that RAECs overexpressing NID1 had the potential to spontaneously form tubular structures (Fig. S9A). In addition, we accidently observed that with increased cell density in the plate, the stacked cells aggregated to form tubules, and the tubule network of RAECs was small and uniform. The tubular structure of the EVs group was relatively thick, and there were single cells distributed in the interstitial space (Fig. S9B). It was speculated that the reduced adhesion strength of the EVs group caused some cells to fall off and then aggregate into tubes. While the tubule characteristics of the EVs^{shNID1} group were similar to those of the RAECs group, further supporting that NID1 promoted the formation of vascular-like structures by reducing the adhesion of RAECs.

The above data indicated that EV-NID1 derived from BMSCs regulates the adhesion and angiogenesis of RAECs by targeting intracellular myosin-10.

3.5. EV-NID1 hydrogel accelerates angiogenesis and promotes bone regeneration

To further dissect and evaluate the therapeutic effect of EV-NID1 *in vivo*, we loaded EVs and EVs^{shNID1} into an alginate/PEG2000/gelatin composite hydrogel and then implanted them into the femoral condylar defects of Sprague-Dawley (SD) rats. Angiogenesis in the defect area was observed at 4 weeks, and bone regeneration was evaluated at 8 weeks post operation (Fig. 5A). The physical characteristics of the hydrogel scaffolds were as follows: the swelling ratio of each group was approximately 14.2% (Fig. S10A), and the hydration degree was approximately 93% (Fig. S10B). The elastic modulus of the material was approximately 120 KPa, and the stress-strain curve was smooth, indicating that the material has uniform structure and good mechanical properties (Fig. S10C). SEM images revealed that a large number of pores were distributed inside the hydrogel, and there was no significant difference in pore size. The magnified image showed that granular EVs were distributed uniformly in the EVs/Hydrogel. The structure of the EVs was intact, and the particle size was consistent with the NTA data (Fig. 5B).

At 4 weeks post operation, HE staining images revealed that the tissue infiltration status in the defect site of the EVs/Hydrogel group was relatively sufficient, the material degraded rapidly and there were more bony connections between the material and the host bone. The interface integration of the EVs^{shNID1}/Hydrogel group was less than that of the EVs/Hydrogel group, and the material degradation rate was relatively slow. In the hydrogel group, the interface between the material and the host bone was mostly connected by fibrous tissue, and the material degradation rate was equivalent to that of the EVs^{shNID1}/Hydrogel group. The defect in the Blank group was filled with cord-like connective tissue (Fig. 5C).

It has been reported that type III collagen is closely associated with angiogenesis and participates in the process of vascular regeneration during the process of wound repair [33]. In this study, sirius red staining showed that the area and proportion of type III collagen in the EVs/Hydrogel group was much higher than those in the other three groups (Fig. 5D and E). The endomucin (EMCN) immunofluorescence and CD31 immunohistochemistry staining showed that EV-NID1 (EVs/hydrogel) recruited more EMCN positive endothelial cells to accumulate at the defect site which leads to more $CD31^+$ capillaries located in the EVs-hydrogel (Figs. S10D and E). Moreover, the number of $CD31^+NID1^+$ (double positive, DP) cells was the highest among these groups. The colocalization of CD31 and NID1 suggested that NID1 played regulatory roles in angiogenesis. The number of $CD31^+$ vessels and DP cells in the EVs^{shNID1}/Hydrogel group was higher than that in the Hydrogel and Blank groups, but still significantly less than those in the EVs/Hydrogel group, indicating that EV-NID1 accelerated angiogenesis in the microenvironment of bone defects (Fig. 5F and G).

Then, we further evaluated the effect of EV-NID1 on bone regeneration. The results of calcein-alizarin red fluorescence double-labeling showed that the osteogenic rate of the EVs/Hydrogel was significantly faster than that of the other three groups. There was no significant difference between the EVs^{shNID1}/Hydrogel and Hydrogel groups, but both of them were faster than the Blank group (Fig. 6A). X-ray imaging showed that the defect boundary of the EVs/Hydrogel group was indistinct, indicating that the bone defect was sufficiently repaired,

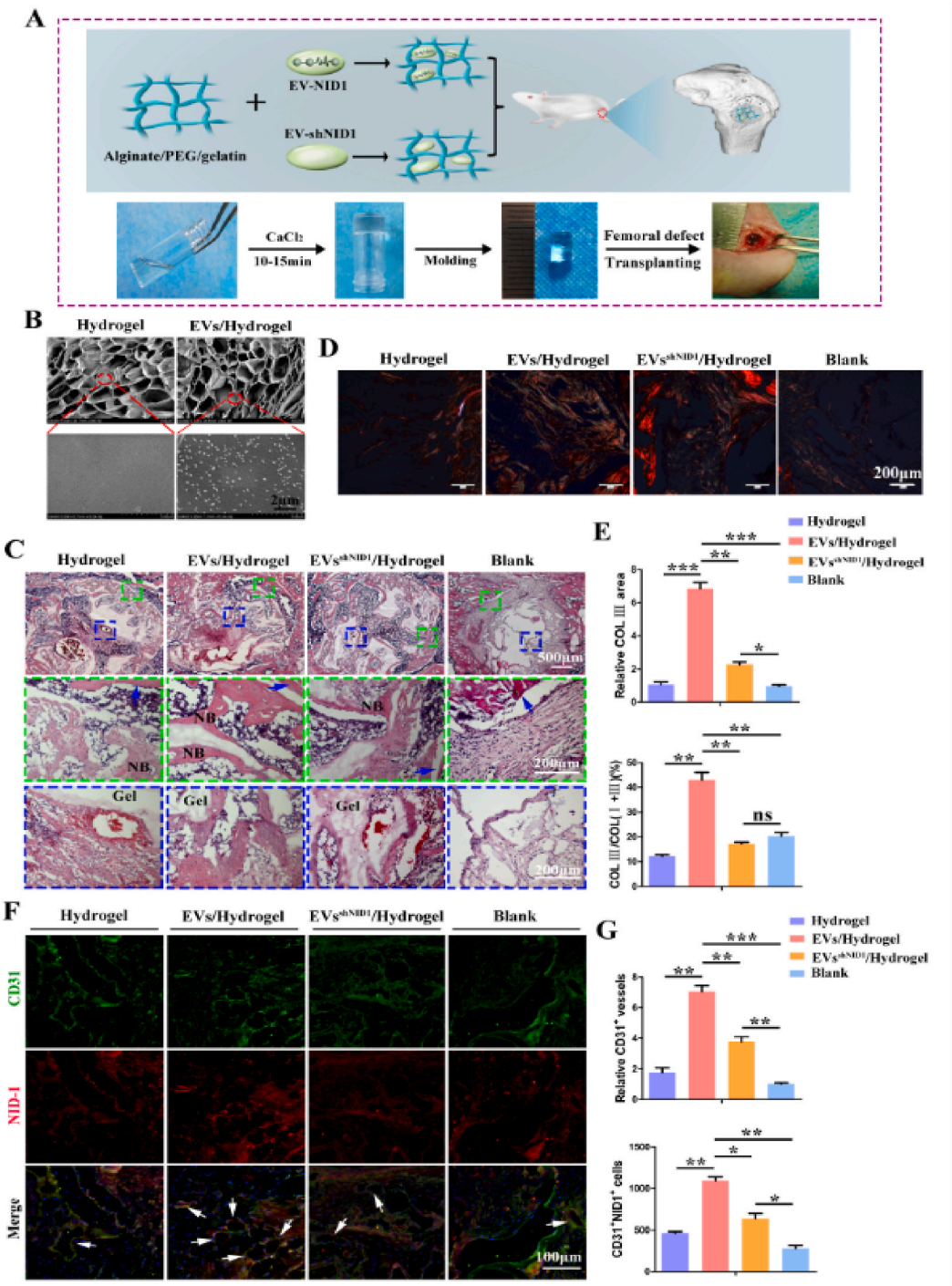

Fig. 5. Hydrogel loaded with EV-NID1 significantly promotes angiogenesis at bone defects sites. (A) Program diagram of the construction and application of EVs-hydrogel. (B) The microstructure and EVs distribution inside hydrogels were characterized by SEM. (C) At 4 weeks post operation, HE staining was used to observe the cell infiltration and the hydrogel degradation at the defect site. The green dashed box represents the integration of the interface between the regenerative tissue and the host bone, and the blue dashed box represents the status of tissue filling and material degradation in the defect center. (D) Sirius red staining showed collagen coverage in the defect area. Under polarized light, red/orange represents typeIcollagen, and green represents type III collagen. Scale bar,200 μm. (E) The relative coverage of type III collagen in the defect area, and the proportion of type III collagen in total typeIand III collagen. (F) Immunofluorescence staining of CD31 and NID1, the white arrow represents the double-positive tubular structure of CD31 and NID1. Scale bar,100 μm. (G) Comparison of the relative number of $CD31^+$ vessels, and count the CD31/NID1 double positive cells. Data were represented as the mean ± SD. *$p < 0.05$; **$p < 0.01$; ***$p < 0.001$; ns, not significant from Student's t-test.

while defects remained in the other three groups (Fig. S11A). The Van Gieson (VG) stained images showed that the new trabecular bone number in the EVs/Hydrogel group was significantly greater than that in the other three groups (Fig. 6B). Micro-CT images, bone volume, trabecular bone number and other analysis data showed that the bone repair status of the EVs/Hydrogel group was significantly better than that of the other three groups, which confirmed the positive effect of EV-NID1 on bone regeneration. Notably, the EVs^{shNID1}/Hydrogel slightly promoted bone regeneration (Fig. 6C and D, Fig. S11B). Immunohistochemical staining of type I collagen (COL I) and osteocalcin (OCN)

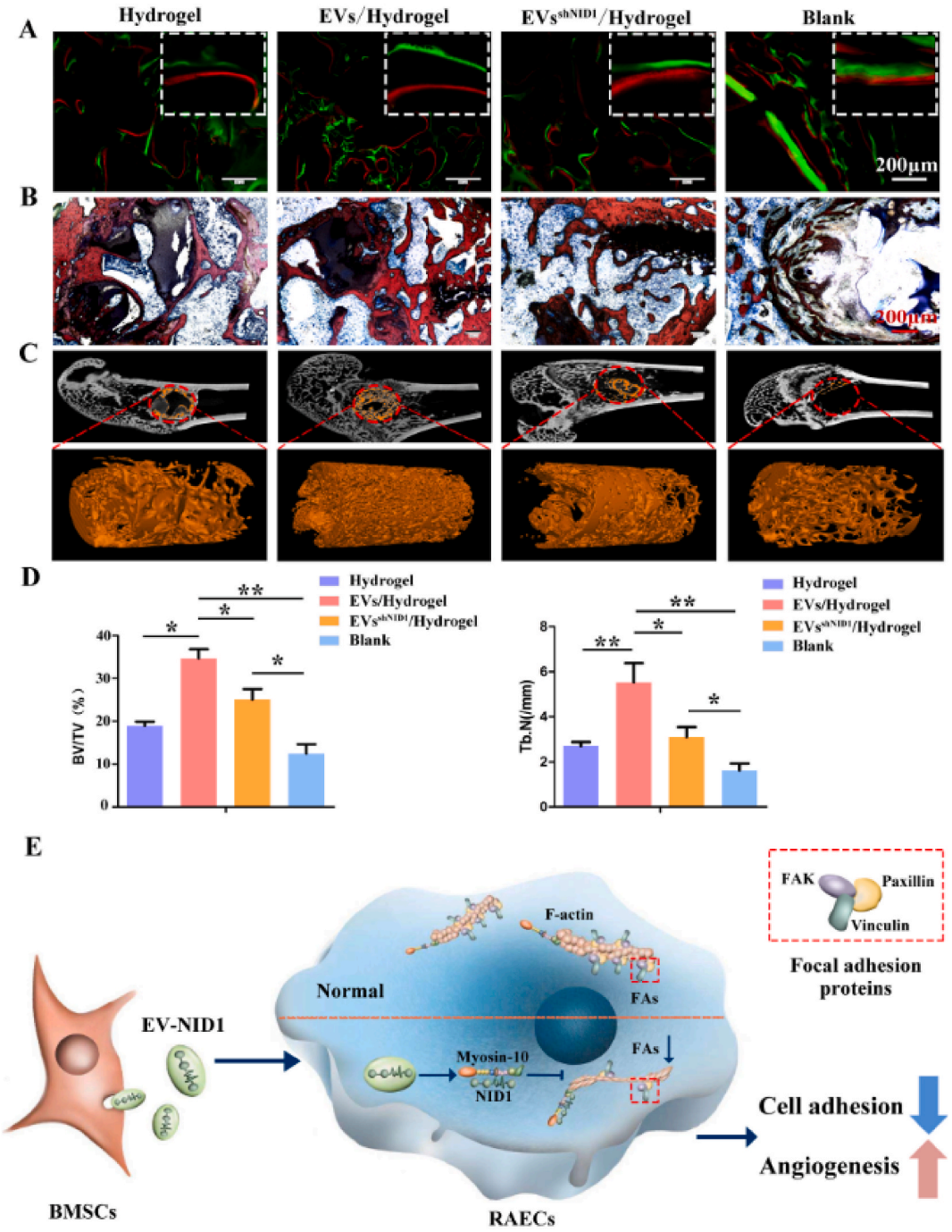

Fig. 6. EV-NID1 loaded hydrogel accelerates bone repair. (A) The bone regeneration rate of the Hydrogel, EVs/Hydrogel, EVs^{shNID1}/Hydrogel and Blank groups were evaluated by calcein (green)/alizarin red (red) fluorescence double labeling. (B) VG staining was performed on the samples without decalcification to observe the distribution of new trabecular bone. (C)Micro-CT analysis image, the red dashed ellipse represents the ROI of the defect area, and the orange column is the 3D reconstruction image of new bone. (D) Bone volume fraction (BV/TV%) and trabecular number (Tb.N) in the reconstruction area of Micro-CT. Data were represented as the mean ± SD. *$p < 0.05$; **$p < 0.01$. (E) The schematic diagram showed the role and mechanism of EV-NID1.

showed that the contribution of EVs/hydrogel to material degradation and bone matrix accumulation was significantly better than that of other groups (Fig. S11C).

In summary, EV-NID1 is internalized by RAECs, and NID1 releases and binds with myosin-10, which triggers cytoskeletal remodeling, reduces the formation and assembly of FAs, and weakens the adhesion strength of RAECs to the ECM, resulting in RAECs more easily migrating and orienting to form a tubular structure, and ultimately accelerating angiogenesis(Fig. 6E). Moreover, the hydrogel scaffold loaded with EV-NID1 significantly accelerates the angiogenesis process and promotes bone regeneration, which is a useful attempt of cell-free treatment. .

4. Discussion

The construction of prevascularized grafts by loading BMSCs is a common strategy to improve the success rate of large bone defect healing [34–36]. However, BMSC transplantation is difficult to widely use in clinical practice due to ethical and safety restrictions [37]. EVs were demonstrated to be an important mediator of intercellular communication, and BMSC-derived EVs are considered to have the

potential to promote angiogenesis and bone regeneration [38–41]. Therefore, cell-free therapies based on EVs have emerged and developed rapidly, and have the potential to be an effective strategy for clinical transformation in the future [21,42,43].

The disadvantage is that the quality and composition of EVs produced under different experimental conditions are not uniform, resulting in inconclusive research on their mechanism, which restricts the therapeutic efficiency and development process of EV biological products. Therefore, accurate identification of effector molecules in EVs, elucidation of regulatory channels and mechanisms, then construction and optimization of tissue engineering grafts with specific targets are the development trends of EV biopharmaceuticals. Here, we found that EVs derived from BMSCs effectively regulate the biological functions of RAECs, and further identified NID1 as the key signaling molecule in BMSC-EVs.

NID1 is a ubiquitous vascular basement membrane (BM) component, whose interactions in particular with laminin, collagen IV and perlecan have been considered important for BM formation and capillary homeostasis [28,44]. In addition to its role as a matrix protein, whether NID1 participates in cell regulation as a signal molecule has not been clearly elucidated. In 2010, it was reported that the laminin deposition and distribution of the β1 and β4 integrin chains were significantly altered during the skin wound healing process in adult NID1 deficient mice, but these differences did not affect the ultrastructural appearance of the BM suggesting a non-structural role for NID1 in wound repair [45]. Moreover, a recent study identified NID1 as a protein enriched in EVs from metastatic hepatocellular carcinoma (HCC) cells by proteomic profiling, and confirmed that EV-NID1 activates fibroblasts to secrete tumor necrosis factor receptor 1 (TNFR1), and facilitate lung colonization of tumor cells [46]. Another study showed that NID1 reduces the cardiomyocyte apoptosis by binding to αvβ3 integrin and beneficially modulates immune responses *in vitro* [29]. These results indicate that NID1 not only supports microvascular architecture, but may also modulate cell properties by binding with extracellular targets.

Our study reported the identification, therapeutic effect and significance of EV-NID1 derived from BMSCs for the first time, discovered that myosin-10 is the intracellular binding target of NID1, and further clarified the approach and mechanism of EV-NID1 to mediate the biological changes of RAECs. Previous results and our findings revealed the functional diversity of NID1, including as a structural component or as a signal molecule interacting with intracellular targets.

Myosin-10 is an actin-based molecular motor that participates in essential intracellular processes such as filopodia formation/extension, phagocytosis, and cell migration [47,48]. Myosin-10 affects the polarity and distribution of stress fibers by targeting FAs, and then regulates cell adhesion, differentiation and cytoskeleton remodeling [49]. Knockdown of myosin-10 results in decreased expression of paxillin and vinculin, while paxillin and vinculin were found to be required primarily for the recruitment of FAK to robust focal adhesions [50,51]. In this study, the expression of myosin-10 decreased in RAECs pretreated with EV-NID1 and other phenotypes were consistent with the above studies. Thus, it is reasonable to suppose that NID1 reduces myosin-10 activity and regulates cell adhesion. Notably, the mechanism by which NID1 reduces the expression of myosin-10 remains unclear, and should be further explored in the future.

A major question in cell biology is how substances (e.g. proteins, RNA and vesicles) are moved around inside cells. Therefore molecular motors are essential, as they result in highly directional movement, and provide highly efficient targeted movement [31,32]. Here, we found that NID1 seemed to guide the directional flow of myosin-10 in the cytoplasm, trigger the polarity distribution of F-actin, and then induce cytoskeletal remodeling and pseudopodia contraction of RAECs.

In addition, EV-NID1 induced cytoskeletal remodeling and ECM degradation of RAECs by upregulating the expression of *Bcl6*, *Mmp10* and *Mmp13*. The above results indicated that the regulation of RAECs by EV-NID1 was hierarchical. The first step was to reduce the formation of FAs and drive cytoskeleton remodeling, so as to accumulate energy for cell migration; Second, EVs induced RAECs to secrete degrading enzymes to decompose the ECM and reduce the resistance of cell migration. As a result, RAECs more easily de-adhere and then migrate to specific locations to participate in angiogenesis.

Bioactive materials loaded with drugs or biomolecules represent an interesting strategy to stimulate osteogenesis and angiogenesis [52]. The generation of a composite of EVs/exosomes and biological carriers to construct tissue engineering grafts is an important approach for preclinical translational research [53–57]. Professor K.cheng's research showed that stents releasing exosomes derived from MSCs in the presence of reactive oxygen species enhance vascular healing in rats with renal ischaemia-reperfusion injury [58].Similarly, exosomes derived from human umbilical cord MSCs were loaded into a hyaluronic acid-based hydrogel and injected into the femoral fracture site of rats. The results showed that the exosome-loaded hydrogel significantly promoted vascular regeneration and fracture repair [38]. To further verify the therapeutic effects of EV-NID1 *in vivo* and evaluate the transformation potential of EV-NID1 loaded grafts, a sodium alginate/-PEG2000/gelatin composite hydrogel enriched with EV-NID1 was developed. Physical characterization showed that the EVs/Hydrogel had a porous structure suitable for cell growth and infiltration. The EVs were evenly distributed inside the scaffold and the structure was complete, which ensured the effectiveness of EVs in subsequent applications. *In vivo* data confirmed that the EVs/Hydrogel sequentially and significantly accelerated angiogenesis and bone defect repair, and NID1 was the core element mediating the therapeutic activity of the EVs/Hydrogel. In addition, the positive effect of NID1 on bone regeneration may be attributed to angiogenesis in situ. The results of these *in vivo* experiments verified the effectiveness of EV-NID1, further confirmed the theory of angiogenesis-osteogenesis coupling [59–61], and provided new targets and perspectives for future clinical vascularization strategies.

5. Conclusion

In summary, we found that EV-NID1 binds intracellular myosin-10, and enhances the migration and angiogenesis activities of RAECs by regulating cell adhesion to the ECM. This novel approach and mechanism will help to further understand the biological function of NID1. Furthermore, a new type of tissue engineering scaffold based on EV-NID1 was successfully developed, which significantly improved the vascularization level and repair efficiency of the graft. This study is compatible with precision medicine trends and has certain application value in the field of vascular regeneration.

CRediT authorship contribution statement

Pengzhen Cheng: Supervision, Formal analysis, Writing – original draft, conceived and supervised the work, performed in vivo experiments, performed in vitro experiments, performed bioinformatics and statistical analyses, contributed to writing the manuscript. **Tianqing Cao:** performed in vitro experiments. **Xueyi Zhao:** performed in vitro experiments. **Huanbo Wang:** performed in vitro experiments.**Weiguang Lu:** performed in vitro experiments. **Sheng Miao:** performed in vivo experiments. **Fenru Ning:** Formal analysis, performed bioinformatics and statistical analyses. **Dong Wang:** performed in vivo experiments. **Yi Gao:** performed in vitro experiments. **Long Wang:** performed in vitro experiments. **Guoxian Pei:** Supervision, conceived and supervised the work. **Liu Yang:** Supervision, Writing – original draft, conceived and supervised the work, contributed to writing the manuscript.

Declaration of competing interest

All authors declare that they have no conflicts of interest and no

competing interest.

Acknowledgements

The authors would like to thank Liyuan Jia and Yaqian Hu for technical support. This work was supported by the National Natural Science Foundation of China (Project no. 81902202, 81772377, 81430049 and 81902263).

Appendix A. Supplementary data

Supplementary data to this article can be found online at https://doi.org/10.1016/j.bioactmat.2021.10.021.

References

[1] C. Wang, M. Wang, T. Xu, X. Zhang, C. Lin, W. Gao, H. Xu, B. Lei, C. Mao, Engineering bioactive self-healing antibacterial exosomes hydrogel for promoting chronic diabetic wound healing and complete skin regeneration, Theranostics 9 (2019) 65–76, https://doi.org/10.7150/thno.29766.

[2] H. Jiang, P. Cheng, D. Li, J. Li, J. Wang, Y. Gao, S. Zhang, T. Cao, C. Wang, L. Yang, G. Pei, Novel standardized massive bone defect model in rats employing an internal eight-hole stainless steel plate for bone tissue engineering, Journal of Tissue Engineering and Regenerative Medicine 12 (2018) e2162–e2171, https://doi.org/10.1002/term.2650.

[3] F. Shang, Y. Yu, S. Liu, L. Ming, Y. Zhang, Z. Zhou, J. Zhao, Y. Jin, Advancing application of mesenchymal stem cell-based bone tissue regeneration, Bioactive materials 6 (2021) 666–683, https://doi.org/10.1016/j.bioactmat.2020.08.014.

[4] A.M. McDermott, S. Herberg, D.E. Mason, J.M. Collins, H.B. Pearson, J. H. Dawahare, R. Tang, A.N. Patwa, M.W. Grinstaff, D.J. Kelly, E. Alsberg, J. D. Boerckel, Recapitulating bone development through engineered mesenchymal condensations and mechanical cues for tissue regeneration, Sci. Transl. Med. 11 (2019), eaav7756, https://doi.org/10.1126/scitranslmed.aav7756.

[5] C. Zheng, J. Chen, S. Liu, Y. Jin, Stem cell-based bone and dental regeneration: a view of microenvironmental modulation, Int. J. Oral Sci. 11 (2019) 23, https://doi.org/10.1038/s41368-019-0060-3.

[6] B. Liu, J. Li, X. Lei, P. Cheng, Y. Song, Y. Gao, J. Hu, C. Wang, S. Zhang, D. Li, H. Wu, H. Sang, L. Bi, G. Pei, 3D-bioprinted functional and biomimetic hydrogel scaffolds incorporated with nanosilicates to promote bone healing in rat calvarial defect model, Mater. Sci. Eng. C 112 (2020) 110905, https://doi.org/10.1016/j.msec.2020.110905.

[7] C. Mao, W. Zhu, Y. Xiang, Y. Zhu, J. Shen, X. Liu, S. Wu, K.M.C. Cheung, K.W. K. Yeung, Enhanced near-infrared photocatalytic eradication of MRSA biofilms and osseointegration using oxide perovskite-based P–N heterojunction, Advanced Science (2021) 2002211, https://doi.org/10.1002/advs.202002211.

[8] J. Le, L. Zhongqun, W. Zhaoyan, S. Yijun, W. Yingjin, W. Yaojie, J. Yanan, J. Zhanrong, M. Chunyang, G. Fangli, X. Nan, Z. Lingyun, W. Xiumei, W. Qiong, L. Xiong, S. Xiaodan, Development of methods for detecting the fate of mesenchymal stem cells regulated by bone bioactive materials, Bioact Mater 6 (2021) 613–626, https://doi.org/10.1016/j.bioactmat.2020.08.035.

[9] P. Cheng, D. Li, Y. Gao, T. Cao, H. Jiang, J. Wang, J. Li, S. Zhang, Y. Song, B. Liu, C. Wang, L. Yang, G. Pei, Prevascularization promotes endogenous cell-mediated angiogenesis by upregulating the expression of fibrinogen and connective tissue growth factor in tissue-engineered bone grafts, Stem Cell Res. Ther. 9 (2018) 176, https://doi.org/10.1186/s13287-018-0925-y.

[10] D. Li, P. Cheng, H. Jiang, T. Cao, J. Wang, Y. Gao, Y. Lin, C. Wang, S. Zhang, J. Li, B. Liu, Y. Song, L. Yang, G. Pei, Vascularization converts the lineage fate of bone mesenchymal stem cells to endothelial cells in tissue-engineered bone grafts by modulating FGF2-RhoA/ROCK signaling, Cell Death Dis. 9 (2018) 959, https://doi.org/10.1038/s41419-018-0999-6.

[11] Y. Hu, L. Chen, Y. Gao, P. Cheng, L. Yang, C. Wu, Q. Jie, A lithium-containing biomaterial promotes chondrogenic differentiation of induced pluripotent stem cells with reducing hypertrophy, Stem Cell Res. Ther. 11 (2020) 77, https://doi.org/10.1186/s13287-020-01606-w.

[12] K. Zhang, X. Zhao, X. Chen, Y. Wei, W. Du, Y. Wang, L. Liu, W. Zhao, Z. Han, D. Kong, Q. Zhao, Z. Guo, Z. Han, N. Liu, F. Ma, Z. Li, Enhanced therapeutic effects of mesenchymal stem cell-derived exosomes with an injectable hydrogel for hindlimb ischemia treatment, ACS Appl. Mater. Interfaces 10 (2018) 30081–30091. https://pubs.acs.org/doi/10.1021/acsami.8b08449.

[13] Z. Shi, Q. Wang, D. Jiang, Extracellular vesicles from bone marrow-derived multipotent mesenchymal stromal cells regulate inflammation and enhance tendon healing, J. Transl. Med. 17 (2019) 211, https://doi.org/10.1186/s12967-019-1960-x.

[14] Y. Nakamura, S. Miyaki, H. Ishitobi, S. Matsuyama, T. Nakasa, N. Kamei, T. Akimoto, Y. Higashi, M. Ochi, Mesenchymal-stem-cell-derived exosomes accelerate skeletal muscle regeneration, FEBS (Fed. Eur. Biochem. Soc.) Lett. 589 (2015) 1257–1265, https://doi.org/10.1016/j.febslet.2015.03.031.

[15] M.Á. Brennan, P. Layrolle, D.J. Mooney, Biomaterials functionalized with MSC secreted extracellular vesicles and soluble factors for tissue regeneration, Adv. Funct. Mater. 30 (2020) 1909125. https://pubmed.ncbi.nlm.nih.gov/32952493/.

[16] F. Diomede, M. D'Aurora, A. Gugliandolo, I. Merciaro, T. Orsini, V. Gatta, A. Piattelli, O. Trubiani, E. Mazzon, Biofunctionalized scaffold in bone tissue repair, Int. J. Mol. Sci. 19 (2018) 1022, https://doi.org/10.3390/ijms19041022.

[17] S. Chen, Y. Tang, Y. Liu, P. Zhang, L. Lv, X. Zhang, L. Jia, Y. Zhou, Exosomes derived from miR-375-overexpressing human adipose mesenchymal stem cells promote bone regeneration, Cell Prolif 52 (2019), e12699, https://doi.org/10.1111/cpr.12669.

[18] J. Xu, Y. Wang, C. Hsu, Y. Gao, C.A. Meyers, L. Chang, L. Zhang, K. Broderick, C. Ding, B. Peault, K. Witwer, A.W. James, Human perivascular stem cell-derived extracellular vesicles mediate bone repair, eLife 8 (2019), e48191. https://elifesciences.org/articles/48191.

[19] A.K. Batsali, A. Georgopoulou, I. Mavroudi, A. Matheakakis, C.G. Pontikoglou, H. A. Papadaki, The role of bone marrow mesenchymal stem cell derived extracellular vesicles (MSC-EVs) in normal and abnormal hematopoiesis and their therapeutic potential, J. Clin. Med. 9 (2020) 856, https://doi.org/10.3390/jcm9030856.

[20] D. Marolt Presen, A. Traweger, M. Gimona, H. Redl, Mesenchymal stromal cell-based bone regeneration therapies: from cell transplantation and tissue engineering to therapeutic secretomes and extracellular vesicles, Frontiers in Bioengineering and Biotechnology 7 (2019) 352, https://doi.org/10.3389/fbioe.2019.00352.

[21] I.M. Bjorge, S.Y. Kim, J.F. Mano, B. Kalionis, W. Chrzanowski, Extracellular vesicles, exosomes and shedding vesicles in regenerative medicine - a new paradigm for tissue repair, Biomater Sci 6 (2017) 60–78, https://doi.org/10.1039/C7BM00479F.

[22] O. Wiklander, M.Á. Brennan, J. Lötvall, X.O. Breakefield, S. Andaloussi, Advances in therapeutic applications of extracellular vesicles, Sci. Transl. Med. 11 (2020) eaav8521, https://doi.org/10.1126/scitranslmed.aav8521.

[23] S. Senapati, V.S. Gnanapragassam, N. Moniaux, N. Momi, S.K. Batra, Role of MUC4–NIDO domain in the MUC4-mediated metastasis of pancreatic cancer cells, Oncogene 31 (2012) 3346–3356, https://doi.org/10.1038/onc.2011.505.

[24] T.R. Patel, C. Bernards, M. Meier, K. McEleney, D.J. Winzor, M. Koch, J. Stetefeld, Structural elucidation of full-length nidogen and the laminin–nidogen complex in solution, Matrix Biol. 33 (2014) 60–67, https://doi.org/10.1016/j.matbio.2013.07.009.

[25] R. Jagroop, C.J. Martin, R.A. Moorehead, Nidogen 1 regulates proliferation and migration/invasion in murine claudin-low mammary tumor cells, Oncol Lett 21 (2021) 52, https://doi.org/10.3892/ol.2020.12313.

[26] M. Balzano, M. De Grandis, T. Vu Manh, L. Chasson, F. Bardin, A. Farina, A. Sergé, G. Bidaut, P. Charbord, L. Hérault, A. Bailly, A. Cartier-Michaud, A. Boned, M. Dalod, E. Duprez, P. Genever, M. Coles, M. Bajenoff, L. Xerri, M. Aurrand-Lions, C. Schiff, S.J.C. Mancini, Nidogen-1 contributes to the interaction network involved in pro-B cell retention in the peri-sinusoidal hematopoietic stem cell niche, Cell Rep. 26 (2019) 3257–3271, https://doi.org/10.1016/j.celrep.2019.02.065, e8.

[27] A. Glentis, V. Gurchenkov, D.M. Vignjevic, Assembly, heterogeneity, and breaching of the basement membranes, Cell Adhes. Migrat. 8 (2014) 236–245, https://doi.org/10.4161/cam.28733.

[28] M. Marchand, C. Monnot, L. Muller, S. Germain, Extracellular matrix scaffolding in angiogenesis and capillary homeostasis, Semin. Cell Dev. Biol. 89 (2019) 147–156, https://doi.org/10.1016/j.semcdb.2018.08.007.

[29] A. Zbinden, S.L. Layland, M. Urbanczyk, D.A. Carvajal Berrio, J. Marzi, M. Zauner, A. Hammerschmidt, E.M. Brauchle, K. Sudrow, S. Fink, M. Templin, S. Liebscher, G. Klein, A. Deb, G.P. Duffy, G.M. Crooks, J.A. Eble, H.K.A. Mikkola, A. Nsair, M. Seifert, K. Schenke Layland, Nidogen-1 mitigates ischemia and promotes tissue survival and regeneration, Advanced Science 8 (2021) 2002500, https://doi.org/10.1002/advs.202002500.

[30] M.J. Boyer, Y. Kimura, T. Akiyama, A.Y. Baggett, K.J. Preston, R. Scalia, S. Eguchi, V. Rizzo, Endothelial cell-derived extracellular vesicles alter vascular smooth muscle cell phenotype through high-mobility group box proteins, J. Extracell. Vesicles 9 (2020) 1781427, https://doi.org/10.1080/20013078.2020.1781427.

[31] D. Tacon, P.J. Knight, M. Peckham, Imaging myosin 10 in cells, BIOCHEM. SOC.T. 32 (2004) 689–693.

[32] I.H. Huang, C.T. Hsiao, J.C. Wu, R.F. Shen, C.Y. Liu, Y.K. Wang, Y.C. Chen, C. M. Huang, A.J. Del, Z.F. Chang, M.J. Tang, K.H. Khoo, J.C. Kuo, GEF-H1 controls focal adhesion signaling that regulates mesenchymal stem cell lineage commitment, J. Cell Sci. 127 (2014) 4186–4200, https://doi.org/10.1242/jcs.150227.

[33] H. Mu, L. Wang, Effect of therapeutic ultrasound on brain angiogenesis following intracerebral hemorrhage in rats, Microvasc. Res. 102 (2015) 11–18, https://doi.org/10.1016/j.mvr.2015.08.001.

[34] B. Sui, C. Hu, A. Liu, C. Zheng, K. Xuan, Y. Jin, Stem cell-based bone regeneration in diseased microenvironments: challenges and solutions, Biomaterials 196 (2019) 18–30, https://doi.org/10.1016/j.biomaterials.2017.10.046.

[35] Z. Li, A. Yang, X. Yin, S. Dong, F. Luo, C. Dou, X. Lan, Z. Xie, T. Hou, J. Xu, J. Xing, Mesenchymal stem cells promote endothelial progenitor cell migration, vascularization, and bone repair in tissue-engineered constructs via activating CXCR2-Src-PKL/Vav2-Rac1, Faseb. J. 32 (2018) 2197–2211, https://doi.org/10.1096/fj.201700895R, fj.201700895R.

[36] J. Nulty, F.E. Freeman, D.C. Browe, R. Burdis, D.P. Ahern, P. Pitacco, Y.B. Lee, E. Alsberg, D.J. Kelly, 3D bioprinting of prevascularised implants for the repair of critically-sized bone defects, Acta Biomater. 126 (2021) 154–169, https://doi.org/10.1016/j.actbio.2021.03.003.

[37] S. Jiang, G. Tian, Z. Yang, X. Gao, F. Wang, J. Li, Z. Tian, B. Huang, F. Wei, X. Sang, L. Shao, J. Zhou, Z. Wang, S. Liu, X. Sui, Q. Guo, W. Guo, X. Li, Enhancement of acellular cartilage matrix scaffold by Wharton's jelly mesenchymal stem cell-

derived exosomes to promote osteochondral regeneration, Bioactive Materials 6 (2021) 2711–2728, https://doi.org/10.1016/j.bioactmat.2021.01.031.
[38] Y. Zhang, Z. Hao, P. Wang, Y. Xia, J. Wu, D. Xia, S. Fang, S. Xu, Exosomes from human umbilical cord mesenchymal stem cells enhance fracture healing through HIF-1α-mediated promotion of angiogenesis in a rat model of stabilized fracture, Cell Prolif 52 (2018), e12570, https://doi.org/10.1111/cpr.12570.
[39] R. Takeuchi, W. Katagiri, S. Endo, T. Kobayashi, Exosomes from conditioned media of bone marrow-derived mesenchymal stem cells promote bone regeneration by enhancing angiogenesis, PLoS One 14 (2019), e0225472, https://doi.org/10.1371/journal.pone.0225472.
[40] P. Chen, L. Zheng, Y. Wang, M. Tao, Z. Xie, C. Xia, C. Gu, J. Chen, P. Qiu, S. Mei, L. Ning, Y. Shi, C. Fang, S. Fan, X. Lin, Desktop-stereolithography 3D printing of a radially oriented extracellular matrix/mesenchymal stem cell exosome bioink for osteochondral defect regeneration, Theranostics 9 (2019) 2439–2459, https://doi.org/10.7150/thno.31017.
[41] S. Zhang, S.J. Chuah, R.C. Lai, J.H.P. Hui, S.K. Lim, W.S. Toh, MSC exosomes mediate cartilage repair by enhancing proliferation, attenuating apoptosis and modulating immune reactivity, Biomaterials 156 (2018) 16–27, https://doi.org/10.1016/j.biomaterials.2017.11.028.
[42] O.G. De Jong, B.W.M. Van Balkom, R.M. Schiffelers, C.V.C. Bouten, M.C. Verhaar, Extracellular vesicles: potential roles in regenerative medicine, Front. Immunol. 5 (2014) 608, https://doi.org/10.3389/fimmu.2014.00608.
[43] M. Zhai, Y. Zhu, M. Yang, C. Mao, Human mesenchymal stem cell derived exosomes enhance cell-free bone regeneration by altering their miRNAs profiles, Advanced Science 7 (2020) 2001334, https://doi.org/10.1002/advs.202001334.
[44] L. Ulazzi, S. Sabbioni, E. Miotto, A. Veronese, A. Angusti, R. Gafa, S. Manfredini, F. Farinati, T. Sasaki, G. Lanza, M. Negrini, Nidogen 1 and 2 gene promoters are aberrantly methylated in human gastrointestinal cancer, Mol. Cancer 6 (2007) 17, https://doi.org/10.1186/1476-4598-6-17.
[45] A. Baranowsky, S. Mokkapati, M. Bechtel, J. Krügel, N. Miosge, C. Wickenhauser, N. Smyth, R. Nischt, Impaired wound healing in mice lacking the basement membrane protein nidogen 1, Matrix Biol. 29 (2010) 15–21, https://doi.org/10.1016/j.matbio.2009.09.004.
[46] X. Mao, S.K. Tey, C.L.S. Yeung, E.M.L. Kwong, Y.M.E. Fung, C.Y.S. Chung, L. Y. Mak, D.K.H. Wong, M.F. Yuen, J.C.M. Ho, H. Pang, M.P. Wong, C.O.N. Leung, T. K.W. Lee, V. Ma, W.C.S. Cho, P. Cao, X. Xu, Y. Gao, J.W.P. Yam, Nidogen 1-enriched extracellular vesicles facilitate extrahepatic metastasis of liver cancer by activating pulmonary fibroblasts to secrete tumor necrosis factor receptor 1, Advanced Science 7 (2020) 2002157, https://doi.org/10.1002/advs.202002157.
[47] Y. Takagi, R.E. Farrow, N. Billington, A. Nagy, C. Batters, Y. Yang, J.R. Sellers, J. E. Molloy, Myosin-10 produces its power-stroke in two phases and moves processively along a single actin filament under low load, Proc. Natl. Acad. Sci. Unit. States Am. 111 (2014) E1833–E1842, https://doi.org/10.1073/pnas.1320122111.
[48] P.F. Liu, Y.H. Wang, Y.W. Cao, H.P. Jiang, X.C. Yang, X.S. Wang, H.T. Niu, Far from resolved: stromal cell-based iTRAQ research of muscle-invasive bladder cancer regarding heterogeneity, Oncol. Rep. 32 (2014) 1489–1496, https://doi.org/10.3892/or.2014.3340.
[49] S.K. Mitra, D.A. Hanson, D.D. Schlaepfer, Focal adhesion kinase: in command and control of cell motility, Nat. Rev. Mol. Cell Biol. 6 (2005) 56–68, https://doi.org/10.1038/nrm1549.
[50] H. Yano, Y. Mazaki, K. Kurokawa, S.K. Hanks, M. Matsuda, H. Sabe, Roles played by a subset of integrin signaling molecules in cadherin-based cell–cell adhesion, JCB (J. Cell Biol.) 166 (2004) 283–295, https://doi.org/10.1083/jcb.200312013.
[51] P.A. Bondzie, H.A. Chen, M.Z. Cao, J.A. Tomolonis, F. He, M.R. Pollak, J. M. Henderson, Non-muscle myosin-IIA is critical for podocyte f-actin organization, contractility, and attenuation of cell motility, Cytoskeleton 73 (2016) 377–395, https://doi.org/10.1002/cm.21313.
[52] L. Casarrubios, A. Polo-Montalvo, M.C. Serrano, M.J. Feito, M. Vallet-Regí, D. Arcos, M.T. Portolés, Effects of ipriflavone-loaded mesoporous nanospheres on the differentiation of endothelial progenitor cells and their modulation by macrophages, Nanomaterials 11 (2021) 1102, https://doi.org/10.3390/nano11051102.
[53] X. Liu, Y. Yang, Y. Li, X. Niu, B. Zhao, Y. Wang, C. Bao, Z. Xie, Q. Lin, L. Zhu, Integration of stem cell-derived exosomes with in situ hydrogel glue as a promising tissue patch for articular cartilage regeneration, Nanoscale 9 (2017) 4430–4438, https://doi.org/10.1039/C7NR00352H.
[54] C. Han, J. Zhou, C. Liang, B. Liu, X. Pan, Y. Zhang, Y. Wang, B. Yan, W. Xie, F. Liu, X.Y. Yu, Y. Li, Human umbilical cord mesenchymal stem cell derived exosomes encapsulated in functional peptide hydrogels promote cardiac repair, Biomater Sci 7 (2019) 2920–2933, https://doi.org/10.1039/C9BM00101H.
[55] L. Chen, S. Mou, F. Li, Y. Zeng, Y. Sun, R.E. Horch, W. Wei, Z. Wang, J. Sun, Self-assembled human adipose-derived stem cell-derived extracellular vesicle-functionalized biotin-doped polypyrrole titanium with long-term stability and potential osteoinductive ability, ACS Appl. Mater. Interfaces 11 (2019) 46183–46196, https://doi.org/10.1021/acsami.9b17015.
[56] Y. Wei, M. Shi, J. Zhang, X. Zhang, K. Shen, R. Wang, R.J. Miron, Y. Xiao, Y. Zhang, Autologous versatile vesicles-incorporated biomimetic extracellular matrix induces biomineralization, Adv. Funct. Mater. 30 (2020) 2000015, https://doi.org/10.1002/adfm. 2000015.
[57] Z. Wu, D. He, H. Li, Bioglass enhances the production of exosomes and improves their capability of promoting vascularization, Bioactive Materials 6 (2021) 823–835, https://doi.org/10.1016/j.bioactmat.2020.09.011.
[58] S. Hu, Z. Li, D. Shen, D. Zhu, K. Huang, T. Su, P. Dinh, J. Cores, K. Cheng, Exosome-eluting stents for vascular healing after ischaemic injury, Nature Biomedical Engineering 5 (2021) 1174–1188, https://doi.org/10.1038/s41551-021-00705-0.
[59] H. Xie, Z. Cui, L. Wang, Z. Xia, Y. Hu, L. Xian, C. Li, L. Xie, J. Crane, M. Wan, G. Zhen, Q. Bian, B. Yu, W. Chang, T. Qiu, M. Pickarski, L. Duong, J.J. Windle, X. Luo, E. Liao, X. Cao, PDGF-BB secreted by preosteoclasts induces angiogenesis during coupling with osteogenesis, Nat. Med. 20 (2014) 1270–1278, https://doi.org/10.1038/nm.3668.
[60] Y. Tang, K. Luo, Y. Chen, Y. Chen, R. Zhou, C. Chen, J. Tan, M. Deng, Q. Dai, X. Yu, J. Liu, C. Zhang, W. Wu, J. Xu, S. Dong, F. Luo, Phosphorylation inhibition of protein-tyrosine phosphatase 1B tyrosine-152 induces bone regeneration coupled with angiogenesis for bone tissue engineering, Bioactive Materials 6 (2021) 2039–2057, https://doi.org/10.1016/j.bioactmat.2020.12.025.
[61] J. Wang, Y. Gao, P. Cheng, D. Li, H. Jiang, C. Ji, S. Zhang, C. Shen, J. Li, Y. Song, T. Cao, C. Wang, L. Yang, G. Pei, CD31hiEmcnhi vessels support new trabecular bone formation at the frontier growth area in the bone defect repair process, SCI REP-UK 7 (2017) 4990, https://doi.org/10.1038/s41598-017-04150-5.